# Plasmonic Nanohole Arrays with Enhanced Visible-light Photoelectrocatalytic Activity

Huaping Jia[1,2,3,4], Zhiyong Li[5], Bingzhe Wang[6], Guichuan Xing[6], Yat Lam Wong[2], Hui Ren[2], Mingjie Li[2], Kwok-Yin Wong[5], Dangyuan Lei[7], Lok-Wing Wong[2], Jiong Zhao[2], Wendong Zhang[1,4], Shengbo Sang[1,4*], Aoqun Jian[1,4*], and Xuming Zhang[2,3*]

[1] Shanxi Key Laboratory of Micro Nano Sensors & Artificial Intelligence Perception, College of Information and Computer, Taiyuan University of Technology, Taiyuan, 030024, China

[2] Department of Applied Physics, The Hong Kong Polytechnic University, Hong Kong, 999077, China

[3] Photonics Research Institute, The Hong Kong Polytechnic University, Hong Kong, 999077, China

[4] Key Lab of Advanced Transducers and Intelligent Control System of the Ministry of Education, Taiyuan University of Technology, Taiyuan, 030024, China

[5] State Key Laboratory of Chemical Biology and Drug Discovery, Department of Applied Biology and Chemical Technology, The Hong Kong Polytechnic University, Hong Kong, 999077, China

[6] Joint Key Laboratory of the Ministry of Education, Institute of Applied Physics and Materials Engineering, University of Macau, Macau, 999078, China

[7] Department of Materials Science and Engineering, City University of Hong Kong, Hong Kong, 999077, China

* Corresponding authors: sunboa-sang@tyut.edu.cn, jianaoqun@tyut.edu.cn, xuming.zhang@polyu.edu.hk

**ABSTRACT:** Metallic nanohole arrays exciting both surface plasmon polariton (SPP) and localized surface plasmon resonance (LSPR) in a single thin film has sparked considerable interest in the field of plasmonics. To exert their full potential for generation of hot electrons in visible light, we bury an Au nanohole array (AuNHA) under a thin $TiO_2$ layer and decorate Pt nanoparticles randomly

on the surface to form the Pt/$TiO_2$/AuNHA nanocomposite. As compared to the Pt/$TiO_2$/Au film, the Pt/$TiO_2$/AuNHA sample with the 90-nm hole diameter obtains the enhancement of 4.1 folds in photocurrent density, 14.7 folds in the peak of incident photon-to-current conversion efficiency (IPCE), and 9.4 folds in degradation of methyl orange. Moreover, numerical simulations are conducted to analyze the contributions of SPP and LSPR effects at different wavelengths. This work is the first study of AuNHA fully covered by a thin $TiO_2$ film and provides a unique design of photoelectrodes for solar photocatalysis applications.

**KEYWORDS:** Au nanohole array, surface plasmon, hot electrons, plasmonic photocatalysis, anodic aluminum oxide (AAO)

The conversion of solar light to chemical energy by using photocatalysts is an economical way toward sustainable economy. As a benchmark material for photocatalysis, titanium dioxide ($TiO_2$) is environmentally friendly, stable, cost-effective, and has a high oxidizing power to decompose unwanted organic compounds.[1] However, its wide bandgap (~3.2 eV) appears to be a major drawback since it makes the material essentially insensitive to visible light which accounts for 54.3% of the energy of sunlight. Several recent studies have shown that the surface plasmon resonance (SPR) effect of noble metal nanostructures can generate hot carriers and significantly enhance the photocatalytic efficiency of wide bandgap semiconductors in visible light, offering an intriguing route toward novel solar energy harvesting devices.[2,3,4] The conversion efficiency lies greatly on the utilization of light-absorption spectral range and charges separation rate.[5,6,7,8,9,10]

In many previous studies, hot electrons are typically generated either by localized surface plasmon resonance (LSPR) in metal nanoparticles (e.g., Au, Ag, and Cu)[11,12,13,14,15] or by surface plasmon polaritons (SPPs) in patterned metal nanostructures.[8] In addition, metal- dielectric-metal (MDM) structures were reported to couple the LSPR mode on Au nanoparticles with the SPP mode on the Au film so as to increase the electric field intensity in the gap between the nanoparticle layer and the metal surface.[8,16] Among various plasmonic metallic nanostructures, nanohole arrays are of

particular interest due to the extraordinary optical properties, superior conductance, high surface-to-volume ratio, and most importantly, the unique plasmonic capability in supporting both the non-propagating LSPR mode and the propagating SPP mode simultaneously.[7,17,18,19,20,21] So far, the metallic nanohole arrays have been intensively applied in biosensing,[22,23] surface enhanced spectroscopy,[24] plasmon-enhanced photovoltaics,[25] metamaterials[26,27], photoelectrocatalysis and electrocatalysis[7,28]. They are usually fabricated by self-colloidal lithography and have the aperture diameter of hundreds nm. Few efforts have been devoted to the plasmonic enhancement of metallic nanohole arrays with diameters below 100 nm in the solar energy conversion field. In this work, we fabricate the Au nanohole arrays (AuNHA) with highly ordered and high-density nanoholes (diameter = 50 nm, 70 nm and 90 nm) in a continuous film by using the anodic aluminum oxide (AAO) template.

In addition, the metallic nanohole arrays can exhibit enhanced optical properties with the deposition of different dielectrics.[2,4,29,30] Atomic layer deposition (ALD) is applied to deposit conformal and highly-uniform $TiO_2$ overlayer, which shows little electronic defects and is beneficial to the transport of plasmon-induced hot electrons. The AuNHA under the thin $TiO_2$ layer can perform dual functions: optical enhancement and high electrical conductivity. The former is due to the support of different plasmonic modes of AuNHA, while the latter is beneficial to the photoelectrochemical process since its continuous metal structure has direct contact with the substrate for easy leading out the photo-excited holes.

Here, we present a nanocomposite Pt/$TiO_2$/AuNHA (from top to bottom) on the FTO substrate to study the SPR effect of size controllable AuNHA in visible light. As the recombination of photo-excited electrons and holes is detrimental to the energy efficiency of photocatalysis, the Pt nanoparticles are deposited on the $TiO_2$ surface as an electron sink to enhance the transfer efficiency of hot electrons.[8] The choice of this structure is to obtain multiple benefits of different layers with the major features include: (i) the enhanced optical extinction (70% - 90%) owing to the co-excitation of

SPP and LSPR modes of AuNHA in visible light; (ii) the improved photon-to-current conversion efficiency (by 14.7 times) since the porous structure of AuNHA has an increased Au/$TiO_2$ interface area for electron transfer and the Au/$TiO_2$ Schottky junction assists the separation of photoexcited electrons and holes; (iii) the raised photoelectrocatalytic (PEC) degradation performance (by 9.4 times) due to SPR effects of AuNHA. With all these merits, the Pt/$TiO_2$/AuNHA nanocomposite is expected to have much-enhanced light-harvesting efficiency and can be applied to a wide range of plasmonic applications.

## RESULTS AND DISCUSSION

**Fabrication and characterization of Pt/$TiO_2$/AuNHA on FTO glass.** The Pt/$TiO_2$/AuNHA nanocomposite consists of three layers: an FTO glass substrate, an AuNHA layer and a $TiO_2$ thin film (from bottom to top, see Figure 1a). In addition, some Pt nanoparticles are decorated on top of the $TiO_2$ film. The AuNHA samples are obtained by transferring from the AAO templates (see Figure 1b). After the fabrication, the nanoholes inherit the regular pattern of the AAO template (see Figure 1c for the overview SEM image of AuNHA(D70) in the area 8 μm × 6 μm). The AuNHA structures have the same thickness of 60 nm and the same interpore distance of 125 nm (i.e., hole period $p$ = 125nm), but have different base diameters (e.g., 50, 70, 90 nm) by using different AAO templates (see Table S1 for the major parameters of samples). Hereafter we use AuNHA(D50), AuNHA(D70), AuNHA(D90) to represent the AuNHA samples with the hole diameters of 50, 70, 90 nm, respectively.

Then, the $TiO_2$ overlayer is coated by the ALD and conformally covers the top surface as well as the sidewalls and bottoms of the nanoholes (see the lower part of Figure 1a). The SEM images and AFM image of $TiO_2$/AuNHA are shown in Figures 1d, S1 and S2. Here the $TiO_2$ overlayer serves dual purposes: the protective layer for AuNHA structure on FTO substrate and the electron filter to separate hot electrons from the underlying AuNHA structure. The thickness of the $TiO_2$ overlayer should be chosen carefully to balance the charge transfer and the film stability. Generally, a thinner

$TiO_2$ film has a shorter distance for the transfer of hot charge carriers and thus higher efficiency, here the $TiO_2$ thickness is chosen to be 15 nm on the trade-off between the durability for PEC reactions and the hot electron transfer efficiency.[12] After the $TiO_2$ deposition, the samples are annealed at 450 $^oC$ for 1 h in the air to ensure that the polycrystalline $TiO_2$ is in the anatase phase (see Figure S3).

The Pt nanoparticles are deposited on the sample surface to promote the electron transfer, which has been verified by many previous studies.[8,31,32,33] The size of Pt nanoparticle clusters can be controlled by adjusting the depositing time of sputtering. As shown by the TEM images in Figure 1e, the Pt nanoparticles remain relatively small and uniform with a diameter of about 2 nm. The EDS elemental analysis of $Pt/TiO_2/AuNHA(D70)$ in Figure S4 further confirms that the Pt nanoparticles are deposited evenly on the sample surface.

**Optical characteristics of AuNHA with and without $TiO_2$ coating in the visible light region.** As stated above, the AuNHAs can support both the LSPR mode and the SPP mode on a given set of experimental conditions.[34,35,36] The simulated spectra of AuNHA are shown in Figure 2a. Here an unpatterned Au film (used as the reference) has a single valley at 500 nm due to the interband transition (*d*-band to *s*-band).[35,37] In comparison, each bare AuNHA has two valleys (near 500 nm and 590 nm) and a strong extinction peak (near 560 nm, see arrows in Figure 2a). It is also observed that the valley near 500 nm presents a slight red-shift with the increase of hole diameter. Since the interband transition is a material property and does not vary with the nanohole geometry, this slight red-shift should be attributed to the SPP effect of AuNHA.[23,38]

It is known that the LSPR peak wavelength and the localized electric field enhancement are highly dependent on the surrounding media.[12,36] In the $TiO_2/AuNHA$ bilayers, the initial single LSPR peaks of the bare AuNHAs near 560 nm now turn into three peaks in 500 – 700 nm as shown in Figure 2b, which actually reflects the coupling of the SPP mode and the LSPR mode at the interface between the AuNHA layer and the 15-nm thick $TiO_2$ overlayer (see the simulated electric fields and the caption of Figure S5). As the AuNHA in the $TiO_2/AuNHA$ bilayer is enclosed by the top $TiO_2$

layer and the FTO substrate, the extinction peaks located at 516 nm, 585 nm and 639 nm (see Figure S5(i)) are induced by the SPR effects in different parts of the AuNHA structure. More specifically, the peak at 516 nm results from the interface between the upper nanohole edge and the $TiO_2$ overlayer, the peak at 585 nm from the upper nanohole film (including the nanohole edge and the neck part of film between adjacent nanoholes) with $TiO_2$ combining the lower nanohole edge with FTO, whereas the peak at 639 nm from the upper nanohole edge with $TiO_2$ combining the lower nanohole edge with FTO. For the fabricated $TiO_2$/AuNHA bilayers, the measured spectra show that the extinction peaks are flattened and smeared (see Figure 2c) but still in the range of 500 – 650 nm as predicted by the simulation. The optical properties of the Pt/$TiO_2$/AuNHA nanocomposites are similar to those of the corresponding $TiO_2$/AuNHA bilayers because the Pt nanoparticles are small and sparse and do not introduce additional plasmonic peaks (see Figure S6).

**Hot-electron transfer mechanism in the Pt/$TiO_2$/AuNHA structure.** Apart from the simulated and measured extinction spectrum, the transient absorption (TA) spectroscopy is applied to study the exciton and carrier dynamics under visible light irradiation[39,40] The TA data for the bare AuNHA(D90), $TiO_2$/AuNHA(D90) and Pt/$TiO_2$/AuNHA(D90) are presented in Figure S7. Upon the excitation of the pump pulse (wavelength 500 nm), the bare AuNHA(D90) shows an excited state absorption (ESA, i.e., $\Delta A > 0$) near 500 nm and a broad negative photo-bleaching (PB, i.e., $\Delta A < 0$) signal in 580 – 700 nm. For the $TiO_2$/AuNHA(D90) sample, an ESA intensity is shown near 500 nm and an additional broad ESA band is observed at ~570 – 700 nm. In contrast, Pt/$TiO_2$/AuNHA(D90) sample shows similar spectral features with $TiO_2$/AuNHA(D90) and a relatively prominent PB signal near 530 nm. Due to the resolution of the measurement, we are unable to trace and compare the plasmon-induced hot-electron excitation difference, but mainly focus on the recombination process. More details are shown in Figure 2d by tracing the PB recovery kinetics, which represents the dynamics of the photogenerated electrons and holes at the band edge including charge recombination, trapping and transfer processes.[41] By comparison, the Pt/$TiO_2$/AuNHA(D90) has a longer lifetime

(1.65 ps) than $TiO_2$/AuNHA(D90) (1.32 ps), indicating that Pt nanoparticles could act as an electron sink to attract the hot electrons to go across $TiO_2$ layer.[42] As the bleaching kinetics of plasmonic nanostructure is strongly laser power-dependent,[43,44] we measured the transient absorptions of $TiO_2$/AuNHA(D90) and Pt/$TiO_2$/AuNHA(D90) under different pump laser power excitations (Figures S7(d) and S7(e)). By fitting the experimental data, it is found that the derived decay times for $TiO_2$/AuNHA(D90) and Pt/$TiO_2$/AuNHA(D90) at 530 nm both increase almost linearly with the pump power as shown in Figure S7(f).

Furthermore, the photoluminescence (PL) spectra of the pure $TiO_2$/AuNHA(D90) sample and three Pt/$TiO_2$/AuNHA samples are compared under the excitation wavelength of 488 nm. It is seen from Figure 2e that all Pt/$TiO_2$/AuNHA samples have similar PL spectral shapes and a much lower PL intensity than the pure $TiO_2$/AuNHA(D90) sample. This suggests that the electrons in the $TiO_2$ conduction band transferred from AuNHA are further moved to the Pt clusters, which suppresses the electron/hole recombination in AuNHA structure. The lower PL emission intensity of Pt/$TiO_2$/AuNHA(D90) than $TiO_2$/AuNHA(D90) is also consistent with the transient absorption analysis of bleaching kinetics in Figure 2d.

Based on the above results and analyses, here we propose Figure 2f to represent the mechanisms of the excitation and transfer of charge carriers in the Pt/$TiO_2$/AuNHA structure under the irradiation of visible light. Since $TiO_2$ is a UV-responsive semiconductor, the visible-light irradiation can only excite the AuNHA layer by the interband transition or the intraband transition.[3,45,46] As the work function of Au is more negative than the Fermi level of $TiO_2$, an internal local electric field is therefore generated.[11,47,48,49] This promotes the transfer of photo-excited electrons to the conduction band of $TiO_2$ by overcoming the Schottky barrier, and then to the Pt nanoparticles on the surface.[50] At the same time, the photo-generated holes are transferred to the FTO substrate.

**Photoelectrochemical performance in the visible region.** In the photoelectrochemical measurements shown in Figure 3a, the Pt/$TiO_2$/AuNHAs are used as the photocathode and are

illuminated by a visible light source (a Xe lamp equipped with a UV cutoff filter $\lambda > 420$ nm). The $Na_2SO_4$ solution (0.5 M) is used as the electrolyte and all samples are normalized to the macroscopic area of 1 $cm^2$. The linear sweep voltammetry (LSV) curves are measured using a scan rate of 5 mV/s in dark and visible light. As one can see from Figure 3b, the Pt/$TiO_2$/AuNHA samples have a larger magnitude of photocurrent density than the control sample of Pt/$TiO_2$/Au film; and among the Pt/$TiO_2$/AuNHA samples, the magnitude of photocurrent density and the onset voltage tends to increase when the nanohole diameter goes larger. Here the pronounced photocurrent and the positive onset potential are beneficial to the overall efficiency of the photocathodic electrode. The LSV curves of $TiO_2$/Au film and $TiO_2$/AuNHA samples are also measured as shown in Figure S8. When compared with Figure 3b, it is seen that the photocurrent densities are greatly enhanced by the deposition of Pt nanoparticles on the sample surface. The transient responses of different samples measured at 0.5 V vs. RHE with and without the light illumination are plotted in Figure 3c. When the Pt/$TiO_2$/Au film is used as the reference, the photocurrent densities of Pt/$TiO_2$/AuNHA(D50), Pt/$TiO_2$/AuNHA(D70), Pt/$TiO_2$/AuNHA(D90) are 3.1, 3.4, and 4.1 times of that of the Pt/$TiO_2$/Au film, respectively (see Table 1 for the values and ratios). However, as shown in Figure S9, the increased surface areas ($\Delta_{Area}$) of AuNHA(D50), AuNHA(D70), AuNHA(D90) with respect to the Au film are $3500\pi N$, $3500\pi N$ and $2700\pi N$ $nm^2$, respectively, here $N$ is the number of the nanoholes in AuNHA. Based on the above data, the photocurrent follows the trend Pt/$TiO_2$/AuNHA(D50) < Pt/$TiO_2$/AuNHA(D70) < Pt/$TiO_2$/AuNHA(D90), whereas the surface area has a different trend Pt/$TiO_2$/AuNHA(D50) = Pt/$TiO_2$/AuNHA(D70) > Pt/$TiO_2$/AuNHA(D90). This suggests that the change of surface area has an ignorable effect, whereas the plasmonic effects of AuNHA is the major reason for the increase of photocurrent. It is also noted that the photocurrent density of the bare Pt/$TiO_2$ film is only 1/21 of that of the Pt/$TiO_2$/Au film. If the bare Pt/$TiO_2$ film is used as the reference, the Pt/$TiO_2$/AuNHA(D90) sample is enhanced by 88.2 times.

As the plasmonic effect is strongly dependent on the wavelength of illumination light, the

photocurrents of different samples are measured when the wavelength is varied at a step of 10 nm by using a monochromator. The results are plotted in Figure S10(a), showing that the photocurrent peaks appear at ~575 nm for all the Pt/$TiO_2$/AuNHA samples. The Pt/$TiO_2$/Au film also shows a weak and broad photocurrent peak in 500 – 700 nm due to the SPR effect caused by the irregularity of Au film deposited on the FTO substrate with a rough surface (see Figure S11).

For a better understanding of the photoelectrocatalytic efficiency, the incident photon-to-electron conversion efficiency (IPCE) is calculated by,

$$\mathrm{IPCE} = \frac{1240 \times I\left(\mathrm{A/cm^2}\right)}{P\left(\mathrm{W/cm^2}\right) \times \lambda\left(\mathrm{nm}\right)} \times 100\,\% \qquad (1)$$

where $I$ and $P$ are the measured photocurrent density and the incident light power density in the units of A/$cm^2$ and W/$cm^2$, respectively, and $\lambda$ is the wavelength in the unit of nm.

In the IPCE curves in Figure 3d, the Pt/$TiO_2$/AuNHA samples show a notable enhancement within the wavelength range of 400−800 nm by comparing with that of the Pt/$TiO_2$/Au film, agreeing with the trends of the photocurrent results in Figures 3b and 3c. Particularly, the Pt/$TiO_2$/AuNHA(D90) sample obtains the maximum efficiency of 0.5% at the peak of ~575 nm, which is 14.7 times that of the Pt/$TiO_2$/Au film (see Table 1). The IPCE curves of all Pt/$TiO_2$/AuNHA samples are relatively flat within the range of 400 – 500 nm and have a broad and obvious IPCE peak after 500 nm, which are not very similar to those of Figure 2c in the general shape. As the reflectance cannot be neglected under irradiation when the incident photon conversion efficiency is considered, we measured the absorption of the samples (see Figure S12). The comparison between the measured IPCE values and absorption spectra of Pt/$TiO_2$/AuNHA(D50), Pt/$TiO_2$/AuNHA(D70) and Pt/$TiO_2$/AuNHA(D90) are shown in Figure S13. Except for the range of 400 – 500 nm in which gold has the high absorption induced by the interband transition, the similar trends of the IPCE and the absorption spectrum of Pt/$TiO_2$/AuNHA over 550 – 800 nm indicate that the enhanced absorption has an impact on the IPCE performance. In addition, the internal quantum

efficiency (IQE) is calculated by dividing the IPCE by absorption to determine the charge separation efficiency as shown in Figure S10(b), which explicitly expresses the fraction of photons absorbed by the electrode that are converted to charge carriers and then give rise to the photocurrent.[9]

To reveal more details about the different mechanisms on the above IPCE performance of $Pt/TiO_2$/AuNHAs, here we will study the enhancements of IPCE and absorption at different wavelengths in visible light. Using the IPCE of the control sample $Pt/TiO_2$/Au film as the reference, we can define the enhancement factor $EF_{\mathrm{IPCE}}$ by

$$EF_{\mathrm{IPCE}} = \frac{\mathrm{IPCE}_{\mathrm{Pt/TiO_2/AuNHA}} - \mathrm{IPCE}_{\mathrm{Pt/TiO_2/Au\ film}}}{\mathrm{IPCE}_{\mathrm{Pt/TiO_2/Au\ film}}} \tag{2}$$

To investigate the contribution of the absorption, we make a similar definition of the enhancement factor of absorption as

$$EF_{abs} = \frac{A_{\mathrm{Pt/TiO_2/AuNHA}} - A_{\mathrm{Pt/TiO_2/Au\ film}}}{A_{\mathrm{Pt/TiO_2/Au\ film}}} \tag{3}$$

here $A_{\mathrm{Pt/TiO_2/AuNHA}}$ and $A_{\mathrm{Pt/TiO_2/Au\ film}}$ represent the absorption intensities of the $Pt/TiO_2$/AuNHA nanocomposite and the $Pt/TiO_2$/Au film, respectively.

Based on the measured IPCE data in Figure 3d, the $EF_{\mathrm{IPCE}}$ of different wavelengths is plotted in Figure 4 for the three $Pt/TiO_2$/AuNHA samples. For easy reference, the corresponding absorption spectra and the calculated $EF_{abs}$ of the $Pt/TiO_2$/AuNHA samples are added into Figure 4 as well. Over the whole range of 400 – 800 nm, although the absorption tends to drop with the increase of wavelength, the $EF_{\mathrm{IPCE}}$ curves are quite flat, with the average values of 7, 8, 12 for $Pt/TiO_2$/AuNHA(D50), $Pt/TiO_2$/AuNHA(D70), $Pt/TiO_2$/AuNHA(D90), respectively. Notably, the $Pt/TiO_2$/AuNHA(D90) sample obtains the highest enhancement. In contrast, the calculated $EF_{abs}$ curves are close to 0 in 400 – 500 nm and then go up at longer wavelengths for all $Pt/TiO_2$/AuNHA samples. Thus, the large $EF_{\mathrm{IPCE}}$ in 400 – 500 nm is not from the enhancement of absorption but other effects as stated below. Although the AuNHA with a larger hole diameter (but a constant hole period

$p$ = 125 nm) has naturally a lower absorption, the average $EF_{IPCE}$ value of Pt/$TiO_2$/AuNHA sample in 400 – 500 nm actually increases with the larger hole diameter. This might be because and the AuNHA with a larger hole diameter has a larger area of hole sidewalls, which is beneficial to the transfer of electrons generated in the interband transition process. Over the wavelength region of 500 – 800 nm, the $EF_{abs}$ and $EF_{IPCE}$ curves of each of the three samples share similar shapes (e.g., peak positions, trend), showing a strong correlation between the IPCE and the absorption. In the other words, in the 500 – 800 nm region, the large $EF_{IPCE}$ may be mainly attributed to the enhanced absorption by the SPR effect of AuNHA.

**Finite-difference time-domain simulation of $TiO_2$/AuNHA.** To analyze the details of plasmonic effects on the IPCE peak, a finite-difference time-domain (FDTD) simulation is conducted on three $TiO_2$/AuNHA bilayers, which correspond to the three measured Pt/$TiO_2$/AuNHA samples with the hole diameters of 50, 70 and 90 nm, respectively. Here the Pt nanoparticles are omitted in the simulations so as to focus on the electric field distributions between $TiO_2$ and AuNHA. The unit cell schemes are shown in the 3D view (Figure 5a) and the XZ view (Figure 5b). In the cross-section of the $TiO_2$/AuNHA bilayer, the locations of two special layers (namely, upper layer and lower layer) are shown as black dash lines in Figure 5c. To investigate the plasmonic response, the normalized electric fields $|E|^2/|E_0|^2$ in the upper layer, the lower layer and the XZ central plane are computed for the three $TiO_2$/AuNHA bilayers (see Figure 5 (d1 – f3)). The wavelength of light is set at 575 nm, which corresponds to the position of the IPCE peak in Figure 3d. The surrounding medium is water (not air) so as to mimic the experimental condition in the photoelectrochemical measurement. In the upper layer as shown in Figure 5(d1) – (d3), the electric field is strong near the edge of holes and on the film between the holes, which represent the LSPR mode and the SPP mode, respectively.[7,19,51] In the lower layer as shown in Figure 5(e1) – (e3), the electric field is strong only near the edge of holes, showing the dominance of the LSPR mode. In the XZ central plane as shown in Figure 5(f1) – (f3), the electric field confirms both SPP and LSPR modes in the upper layer and single LSPR mode in

the lower layer. Since the interpore distance of nanoholes is kept the same, the distance between adjacent hole edges becomes smaller when the hole diameter of AuNHA is increased. When the three samples are compared, the $TiO_2$/AuNHA(D90) bilayer shows the best electric field (see Figure 5(d3) and (f3)) due to the nanoholes with smaller distance in the array structures have the stronger coupling effects of the LSPR mode and the SPP mode.[52,53]

As the wavelength has a strong influence on the plasmonic effects, the simulated electric field of $TiO_2$/AuNHA(D90) bilayer at 575 nm is compared with those at two neighboring extinction dips at 565 nm and 622 nm (see Figure S14). It is obvious that the $TiO_2$/AuNHA(D90) exerts both the SPP mode and the LSPR mode at 575 nm; comparatively, the SPP mode on the film between the adjacent nanoholes[35] is dominant at 565 nm and the LSPR mode at the nanohole edge is the only major factor at 622 nm. To further elucidate the plasmonic response to the broadband light, we have simulated the dynamic response of the $TiO_2$/AuNHA(D90) bilayer to a pulse of visible light ($\lambda > 420$ nm). As shown in the Movie S1 and Figure S15, both the SPP and the LSPR are prominent most of the time, and the LSPR gradually becomes dominant at the hole edges before the electric field fades away eventually.

**Photoelectrocatalytic organic decomposition in visible light.** To evaluate the size controllable AuNHA on the catalytic activity of Pt/$TiO_2$/AuNHA, the decompositions of methyl orange (MO) are performed in neutral aqueous solutions (see details in the Methods Section). Upon the irradiation, the AuNHA generates the electron-hole pairs (see Figures 2f and 3a). The holes are migrated toward the counter electrode via the external connection and typically form hydroxyl radicals •OH, whereas the electrons are transported to the surface of the working electrode and mainly reduce the dissolved oxygen to superoxide $\bullet O_2^-$ anions. These species have sufficient oxidation power (redox potential) to decompose the MO molecules in the electrolyte.[54]

From the measured UV-vis absorbance spectra by the PEC degradation shown in Figure S16, the characteristic absorption peak of MO near 464 nm diminishes gradually with the increase of

irradiation time. The conversion $1 - C/C_0$ as a function of time is plotted in Figure 6a, here $C$ and $C_0$ denote the remnant and initial concentrations of MO, respectively. After the visible-light irradiation for 60 min, the conversion of MO molecules reaches 1.5% by Pt/$TiO_2$, 8.5% by Pt/$TiO_2$/Au film, 32.6% by Pt/$TiO_2$/AuNHA(D50), 43.6% by Pt/$TiO_2$/AuNHA(D70), and 54.4% by Pt/$TiO_2$/AuNHA(D90), respectively. The ascending order of the conversions of the five samples corresponds faithfully to that of the photocurrent density measured in the electrolyte containing MO (40 μM) and $Na_2SO_4$ (0.5 M) (see Figure S17), showing that higher photocurrent indeed leads to more degradation.

When the degradation curves are plotted in the logarithm scale, they present linearity with respect to the reaction time (see Figure 6b). This suggests that the PEC obeys the first-order reaction kinetics as expressed by $C = C_0 \exp(-kt)$, or equivalently $\ln(C_0/C) = kt$, where $k$ is the reaction rate constant. The fitting results are listed in Table 1 as well. Using the Pt/$TiO_2$/Au film as the reference, the Pt/$TiO_2$/AuNHA samples show larger $k$ values with the ratios of 4.8, 6.8 and 9.4 when the AuNHA hole diameters are 50, 70 and 90 nm, respectively. Again, the Pt/$TiO_2$/AuNHA(D90) yields the best performance. In comparison, the Pt/$TiO_2$ structure shows a reduced ratio of 1/6.

To examine the contributions of the SPR effect in visible light, we further test the electrocatalytic process (EC) using the Pt/$TiO_2$/AuNHA(D90), which has the best performance in photocurrent and PEC degradation. According to the measured data in Figure 6c, the MO degradation in PEC is always higher than in EC. In terms of the reaction rate constant shown in Figure 6d, the $k$ value of degradation in PEC is 13 times than that in EC (i.e., $1.32\times10^{-2}$ $min^{-1}$ vs. $1.02\times10^{-3}$ $min^{-1}$). This demonstrates that the SPR effect of AuNHA plays an important role in MO degradation in visible light.

## CONCLUSIONS

In summary, the photocathodic nanocomposite of Pt/$TiO_2$/AuNHA has shown superior photoelectrocatalytic performance in visible light as verified by the measurements of photocurrent,

IPCE and degradation of methyl orange. Both the experimental and simulation studies demonstrate that the enhanced performances result from the plasmonic effects of different parts of the structures and their combined effects. The AuNHA layer exerts both the LSPR mode and the SPP mode simultaneously to enhance the optical absorption; its nanohole structure facilitates the efficient transfer of generated electrons leads to a significant increase in the incident photon-to-electron conversion efficiencies; its direct contact with the $TiO_2$ overlayer generates the Schottky junction to enhance the separation of photo-excited electrons and holes; the Pt nanoparticles work as electron traps to increase the lifetime of hot charge carriers and to promote the transfer of photoexcited electron. Equipped with these favorable features, this nanocomposite is highly potential to boost the solar energy conversion efficiency in applications such as optoelectronic devices, solar cells, and other photo-assisted reactions.

## METHODS

**Fabrication procedures.** The substrate FTO glasses were degreased ultrasonically in acetone, isopropanol, anhydrous ethanol and deionized (DI) water for 10 minutes successively. The AuNHA structure was fabricated by a lift-off process on the anodic aluminum oxide (AAO) template. (1) The AAO template was fixed on a glass slide by using two small pieces of glasses to press at the edges. (2) A 60-nm thick Au film was deposited on the AAO templates by the E-beam system (pressure $4\times 10^{-6}$ Torr). Here the deposition rate of Au was constantly controlled at 0.01 nm/s. (3) The Au-deposited AAO template was transferred to the surface of a NaOH solution (0.1 M). After 20 minutes, the AAO template layer was dissolved, leaving only the AuNHA structure that floated on the water surface. (4) The AuNHA structure film was then manually transferred to a clean FTO glass after being cleaned in the deionized (DI) water. By drying in air with the residual amount of water removed from the interface of the metal, the AuNHA film was attached to the FTO substrate. As a reference sample, the Au film with a thickness of 60 nm was also deposited on the FTO by the E-beam system.

The $TiO_2$ layer was fabricated by Atomic Layer Deposition (ALD, Ultratech), in which $TiCl_4$ and $H_2O$ were used as precursors. The substrate temperature was set as 100℃ and the working pressure was 3 mTorr. The deposition was performed with cycles of $TiCl_4$ (0.1 s pulse), $N_2$ purges (10 s), $H_2O$ (0.015 s pulse) and $N_2$ purges (10 s). The deposition rate was 0.055 nm per cycle.

A magnetron sputtering system (Denton Explorer 14 Sputtering System) was used to deposit Pt nanoparticles on the surface of the $TiO_2$ overlayer. The thickness was controlled by changing the deposition time. When the sputtering time was less than about 100 s, the deposited Pt film was discontinuous, mostly in the form of Pt nanoparticles. Here, Pt nanoparticles were deposited by the RF magnetron sputtering (power 30 W, 50 s) at $4 \times 10^{-6}$ Torr in Ar atmosphere.

**Characterization: SEM, TEM, AFM, XRD, extinction spectrum, PL and TA.** The nanostructure of the as-prepared electrode was characterized by the scanning electron microscope (SEM, JEOL JSM-6335F) and transmission electron microscopy (TEM, JEOL JEM-2011). Surface morphology images were collected in the noncontact mode of atomic force microscope (AFM, Park systems NX10) by using a silicon cantilever (SI-DF20, Seiko Instruments, Japan). The phase of the samples was identified by an X-ray diffractometer (Shimadzu LabX XRD-6000) employing Cu $K_\alpha$ radiation at 40 kV and 30 mA over the $2\theta$ range of 20–80°. The optical properties were monitored using a Perkin-Elmer Lambda 950 UV/vis/NIR. With the transmittance results, the extinction was calculated by extinction = $1 - T$. The photoluminescence (PL) spectra were recorded using the Edinburgh Photoluminescence spectrophotometer. The excitation wavelength was 488 nm, and the photoluminescence spectra were recorded over the range of 620–800 nm. The broadband femtosecond transient absorption (TA) measurements were performed by using the Ultrafast System HELIOS TA spectrometer. The laser source was the Coherent Legend regenerative amplifier (150 fs, 1 kHz, 800 nm) seeded by a Coherent Vitesse oscillator (100 fs, 80 MHz). The broadband probe pulses (400-800 nm) were generated by focusing a small portion of the fundamental 800 nm laser pulses into a 2 mm $CaF_2$ plate. 500 nm pump pulses were generated from a Light Conversion

TOPAS-C optical parametric amplifier.

**Material characterization: Photocurrent density, IPCE and MO (methyl orange) degradation.** PEC measurements were carried out in a standard three-electrode system, consisting of the working electrode, a saturated Ag/AgCl reference electrode and a Pt wire counter electrode. It was carried out by an electrochemical station (CHI 660E, Shanghai Chenhua, China). The photocurrent was measured under the irradiation of a Xenon lamp (100 mW/cm$^2$) fixed with a UV cutoff filter ($\lambda > 420$ nm). The applied potential was referred to the RHE using the following equation:

$$E(\text{vs. RHE}) = E(\text{vs. Ag/AgCl}) + 0.197 + 0.0591 * \text{pH} \quad (4)$$

For the IPCE measurement, the photocurrent was recorded at a constant bias (0.5 V vs. RHE) with a spectral step of 10 nm by a monochromator (Newport). The incident light intensity was measured by an optical power and energy meter (Thorlabs). For accurate measurement, the sensor of the spectroradiometer was placed inside the glass reactor to mimic the intensity at the electrode under experimental conditions. In this way, the intensity loss due to the scattering and absorption of the glass reactor wall was taken into consideration.

For the degradation process, the electrolyte (20 ml) consisted of MO (40 μM) and $Na_2SO_4$ (0.5 M). Before the light irradiation, it was stirred for 30 min to reach the adsorption equilibrium in dark. For the PEC and EC degradations, the prepared samples were used as the working electrode, together with the Ag/AgCl reference electrode and the Pt wire counter electrode. A bias voltage of 0.5V vs. RHE was applied by the electrochemical station (CHI 660E, Shanghai Chenhua, China). After the dark adsorption, the whole reactor was illuminated by a Xeon lamp (100 mW/cm$^2$) with a UV cutoff filter (> 420 nm) for the PEC test, whereas the reactor was kept in dark for the EC test. Finally, the MO decomposition rate was characterized by measuring its concentration using a UV–vis spectrometer (Perkin-Elmer Lambda 950) with the $Na_2SO_4$ (0.5 M) solution as the reference sample.

**Finite-difference time-domain simulation.** A commercial FDTD simulation package (FDTD Solutions, Lumerical Solutions Inc.) was used to calculate the near-field distributions of the

$TiO_2$/AuNHA bilayers. The distance was 200 nm between the excitation plane and the top of the model for reflection. A normally incident plane-wave source with the polarization along the *x*-axis was used to illuminate the AuNHAs. The *x* and *y* ranges of simulation space were set to be the unit cell of the AuNHAs according to the experimental data. The anti-symmetric boundary conditions were used for $x_{min}$ and $x_{max}$, the symmetric boundary conditions were used for $y_{min}$ and $y_{max}$. The $z_{max}$ value was set to be 300 nm away from the top of the model and the $z_{min}$ value was set to be 300 nm away from the bottom of the AuNHAs. The *z* dimension was truncated by the perfectly matched layers. The simulation time was set to be 1000 fs and the time step was set to be the default parameters of the software, the auto-shutoff min value was set to be $1\times10^{-7}$. The mesh size for the model region was set to be 1.0 nm, while the other region was set to be the mesh accuracy of 2. The mesh refinement setting was set to be conformal variant 1. The dielectric functions were modeled using the CRC data for Au, the reference data for FTO[55] and the Devore data for $TiO_2$.[56] The Refractive index of air was set to be 1, and the corresponding extinction coefficients were 0.

## ASSOCIATED CONTENT

### Supporting Information

The Supporting Information is available free of charge at https://pubs.acs.org/doi/...

Parameters of the samples; SEM images of AuNHAs and $TiO_2$/AuNHAs; AFM image and surface profile of $TiO_2$/AuNHA(D70); XRD patterns Pt/$TiO_2$/AuNHA; EDS elemental analysis of Pt/$TiO_2$/AuNHA(D70); Calculated results of the normalized electric field of the $TiO_2$/AuNHA(D90); Comparison of the transmittance spectra of $TiO_2$ and Pt/$TiO_2$; Transient absorption spectra of Pt/$TiO_2$/AuNHA(D90); The LSV curves of $TiO_2$/AuNHAs and $TiO_2$/Au film; Schematic diagram of Au nanohole arrays ; Photocurrent densities and IQE values; SEM images of the FTO surface and the Au film/FTO; The absorption spectra of Pt/$TiO_2$/AuNHAs and Pt/$TiO_2$/Au film; Comparison of the measured IPCE values and the absorption spectra of Pt/$TiO_2$/AuNHAs; Calculated electric field in

the upper layer of the $TiO_2$/AuNHA(D90); Interpretation of the Movie S1; Measured UV-vis absorbance spectra of the PEC degradation; The photocurrent densities measured in the presence of MO (40 μM) and $Na_2SO_4$ (0.5 M) (**PDF**)

Movie S1: The simulated dynamic response of the $TiO_2$/AuNHA(D90) bilayer to the irradiation of broadband visible light ($\lambda$ > 420 nm) (**MP4**)

## AUTHOR INFORMATION


**Corresponding Authors**

*E-mail: sunboa-sang@tyut.edu.cn, jianaoqun@tyut.edu.cn, xuming.zhang@polyu.edu.hk.


**Author Contributions**

H.J. conducted the experiments, processed the data, drafted and revised the manuscript. Z.L. contributed to the numerical simulations, B.W., G.X., H.R. and M.L. performed the transient absorption measurements and analyzed the data, Y.L.W., L.W.W. and J.Z. assisted the characterizations and the nanomaterial preparations, K.Y.W., D.L. and W.Z. contributed to the theoretical analyses, S.S. and A.J. conceived the design and coordinated the research, X.Z. provided the initial idea, supervised the research, revised and finalized the manuscript. All authors read and approved the final manuscript.

**Notes**

The authors declare no competing financial interest.

## ACKNOWLEDGMENTS


This work is supported by the Research Grants Council (RGC) of Hong Kong (15218415, 15212717, 15212618, 15304519, 15215620, N_PolyU511/20), The Hong Kong Polytechnic University (1-ZE14 and 1-ZVGH), and the Innovation and Technology Commission (ITC) of Hong Kong. It is also financially supported by the National Natural Science Foundation of China (61971301, 51622507, 62031022), 863 project of China (2015AA042601), and Excellent Talents Technology Innovation

Program of Shanxi Province (201805D211021). The technical assistance and facility support from Materials Research Centre, and University Research Facility in Material Characterization and Device Fabrication of Hong Kong Polytechnic University are greatly appreciated.

**Funding Sources**

Research Grants Council, University Grants Committee Hong Kong (15218415, 15212717, 15212618, 15304519, 15215620, N_PolyU511/20); Hong Kong Polytechnic University (1-ZE14, 1-ZVGH); National Natural Science Foundation of China (61971301, 51622507, 62031022); National High-tech Research and Development Program “863 Project of China” (2015AA042601); Excellent Talents Technology Innovation Program of Shanxi Province (201805D211021).

## REFERENCES

(1) Zhao, Y.; Hoivik, N.; Wang, K. Recent Advance on Engineering Titanium Dioxide Nanotubes for Photochemical and Photoelectrochemical Water Splitting. Nano Energy **2016**, 30, 728–744.

(2) Im, H.; Lindquist, N. C.; Lesuffleur, A.; Oh, S. Atomic Layer Deposition of Dielectric Overlayers for Enhancing the Optical Plasmonic Nanoholes. ACS Nano **2010**, 4, 947–954.

(3) Tagliabue, G.; Jermyn, A. S.; Sundararaman, R.; Welch, A. J.; DuChene, J. S.; Pala, R.; Davoyan, A. R.; Narang, P.; Atwater, H. A. Quantifying the Role of Surface Plasmon Excitation and Hot Carrier Transport in Plasmonic Devices. Nat. Commun. **2018**, 9, 3394.

(4) Im, H.; Lee, S. H.; Wittenberg, N. J.; Johnson, T. W.; Lindquist, N. C.; Nagpal, P.; Norris, D. J.; Oh, S. H. Template-Stripped Smooth Ag Nanohole Arrays with Silica Shells for Surface Plasmon Resonance Biosensing. ACS Nano **2011**, 5, 6244–6253.

(5) Kim, H. J.; Lee, S. H.; Upadhye, A. A.; Ro, I.; Tejedor-Tejedor, M. I.; Anderson, M. A.; Kim, W. B.; Huber, G. W. Plasmon-Enhanced Photoelectrochemical Water Splitting with Size-Controllable Gold Nanodot Arrays. ACS Nano **2014**, 8, 10756–10765.

(6) Lee, J.; Mubeen, S.; Ji, X.; Stucky, G. D.; Moskovits, M. Plasmonic Photoanodes for Solar Water Splitting with Visible Light. Nano Lett. **2012**, 12, 5014–5019.

(7) Li, J.; Cushing, S. K.; Zheng, P.; Meng, F.; Chu, D.; Wu, N. Plasmon-Induced Photonic and Energy-Transfer Enhancement of Solar Water Splitting by a Hematite Nanorod Array. Nat. Commun. **2013**, 4, 2651.

(8) Hoang, C. V.; Hayashi, K.; Ito, Y.; Gorai, N.; Allison, G.; Shi, X.; Sun, Q.; Cheng, Z.; Ueno, K.; Goda, K.; Misawa, H. Interplay of Hot Electrons from Localized and Propagating Plasmons. Nat. Commun. **2017**, 8, 771.

(9) Yalavarthi, R.; Mascaretti, L.; Kudyshev, Z. A.; Dutta, A.; Kalytchuk, S.; Zbořil, R.; Schmuki, P.; Shalaev, V. M.; Kment, Š.; Boltasseva, A.; Naldoni, A. Enhancing Photoelectrochemical Energy Storage by Large-Area CdS-Coated Nickel Nanoantenna Arrays. ACS Appl. Energy Mater. **2021**, 4, 11367–11376.

(10) Mascaretti, L.; Dutta, A.; Kment, Š.; Shalaev, V. M.; Boltasseva, A.; Zbořil, R.; Naldoni, A. Plasmon‐Enhanced Photoelectrochemical Water Splitting for Efficient Renewable Energy Storage. Adv. Mater. **2019**, 31, 1805513.

(11) Zhang, X.; Chen, Y. L.; Liu, R.-S.; Tsai, D. P. Plasmonic Photocatalysis. Reports Prog. Phys. **2013**, 76, 046401.

(12) Wu, B. H.; Liu, W. T.; Chen, T. Y.; Perng, T. P.; Huang, J. H.; Chen, L. J. Plasmon-Enhanced Photocatalytic Hydrogen Production on Au/$TiO_2$ Hybrid Nanocrystal Arrays. Nano Energy **2016**, 27, 412–419.

(13) Sellappan, R.; Nielsen, M. G.; González-Posada, F.; Vesborg, P. C. K.; Chorkendorff, I.; Chakarov, D. Effects of Plasmon Excitation on Photocatalytic Activity of Ag/$TiO_2$ and Au/$TiO_2$ Nanocomposites. J. Catal. **2013**, 307, 214–221.

(14) Chan, G. H.; Zhao, J.; Hicks, E. M.; Schatz, G. C.; Van Duyne, R. P. Plasmonic Properties of Copper Nanoparticles Fabricated by Nanosphere Lithography. Nano Lett. **2007**, 7, 1947–1952.

(15) Lee, C.; Park, Y.; Park, J. Y. Hot Electrons Generated by Intraband and Interband Transition Detected Using a Plasmonic Cu/$TiO_2$ Nanodiode. RSC Adv. **2019**, 9, 18371–18376.

(16) Shi, X.; Ueno, K.; Oshikiri, T.; Sun, Q.; Sasaki, K.; Misawa, H. Enhanced Water Splitting under Modal Strong Coupling Conditions. Nat. Nanotechnol. **2018**, 13, 953–958.

(17) Ebbesen, T. W.; Lezec, H. J.; Ghaemi, H. F.; Thio, T.; Wolff, P. A. Extraordinary Optical Transmission through Sub-Wavelenght Hole Arrays. Nature **1998**, 391, 667–669.

(18) Ai, B.; Wang, Z.; Möhwald, H.; Zhang, G. Plasmonic Nanochemistry Based on Nanohole Array. ACS Nano **2017**, 11, 12094–12102.

(19) Hajebifard, A.; Berini, P. Fano Resonances in Plasmonic Heptamer Nano-Hole Arrays. Opt. Express **2017**, 25, 18566.

(20) Qiu, T.; Luo, B.; Akinoglu, E. M.; Yun, J.; Gentle, I. R.; Wang, L. Trilayer Nanomesh Films with Tunable Wettability as Highly Transparent, Flexible, and Recyclable Electrodes. Adv. Funct. Mater. **2020**, 30, 2002556.

(21) Bley, K.; Semmler, J.; Rey, M.; Zhao, C.; Martic, N.; Klupp Taylor, R. N.; Stingl, M.; Vogel, N. Hierarchical Design of Metal Micro/Nanohole Array Films Optimizes Transparency and Haze Factor. Adv. Funct. Mater. **2018**, 28, 1–11.

(22) Larson, S.; Carlson, D.; Ai, B.; Zhao, Y. The Extraordinary Optical Transmission and Sensing Properties of Ag/Ti Composite Nanohole Arrays. Phys. Chem. Chem. Phys. **2019**, 21, 3771–3780.

(23) Xiong, K.; Emilsson, G.; Dahlin, A. B. Biosensing Using Plasmonic Nanohole Arrays with Small, Homogenous and Tunable Aperture Diameters. Analyst **2016**, 141, 3803–3810.

(24) Masson, J. F.; Murray-Méthot, M. P.; Live, L. S. Nanohole Arrays in Chemical Analysis: Manufacturing Methods and Applications. Analyst **2010**, 135, 1483–1489.

(25) Menezes, J. W.; Ferreira, J.; Santos, M. J. L.; Cescato, L.; Brolo, A. G. Large-Area Fabrication of Periodic Arrays of Nanoholes in Metal Films and Their Application in Biosensing and Plasmonic-Enhanced Photovoltaics. Adv. Funct. Mater. **2010**, 20, 3918–3924.

(26) Shalaev, V. M. Optical Negative-Index Metamaterials. Nat. Photonics **2007**, 1, 41–48.

(27) Xiong, K.; Emilsson, G.; Maziz, A.; Yang, X.; Shao, L.; Jager, E. W. H.; Dahlin, A. B.

Plasmonic Metasurfaces with Conjugated Polymers for Flexible Electronic Paper in Color. Adv. Mater. **2016**, 28, 9956–9960.

(28) Pang, L.; Barras, A.; Mishyn, V.; Heyte, S.; Heuson, E.; Oubaha, H.; Sandu, G.; Melinte, S.; Boukherroub, R.; Szunerits, S. Plasmon-Driven Electrochemical Methanol Oxidation on Gold Nanohole Electrodes. ACS Appl. Mater. Interfaces **2020**, 12, 50426–50432.

(29) Stelling, C.; Fossati, S.; Dostalek, J.; Retsch, M. Surface Plasmon Modes of Nanomesh-on-Mirror Nanocavities Prepared by Nanosphere Lithography. Nanoscale **2018**, 10, 17983–17989.

(30) Li, Q.; Li, Z.; Wang, X.; Wang, T.; Liu, H.; Yang, H.; Gong, Y.; Gao, J. Structurally Tunable Plasmonic Absorption Bands in a Self-Assembled Nano-Hole Array. Nanoscale **2018**, 10, 19117–19124.

(31) Khaselev, O.; Turner, J. A. A Monolithic Photovoltaic-Photoelectrochemical Device for Hydrogen Production via Water Splitting. Science (80-. ). **1998**, 280, 425–427.

(32) Mubeen, S.; Lee, J.; Singh, N.; Krämer, S.; Stucky, G. D.; Moskovits, M. An Autonomous Photosynthetic Device in Which All Charge Carriers Derive from Surface Plasmons. Nat. Nanotechnol. **2013**, 8, 247–251.

(33) Dasgupta, N. P.; Liu, C.; Andrews, S.; Prinz, F. B.; Yang, P. Atomic Layer Deposition of Platinum Catalysts on Nanowire Surfaces for Photoelectrochemical Water Reduction. J. Am. Chem. Soc. **2013**, 135, 12932–12935.

(34) Live, L. S.; Dhawan, A.; Gibson, K. F.; Poirier-Richard, H. P.; Graham, D.; Canva, M.; Vo-Dinh, T.; Masson, J. F. Angle-Dependent Resonance of Localized and Propagating Surface Plasmons in Microhole Arrays for Enhanced Biosensing. Anal. Bioanal. Chem. **2012**, 404, 2859–2868.

(35) Schwind, M.; Kasemo, B.; Zorić, I. Localized and Propagating Plasmons in Metal Films with Nanoholes. Nano Lett. **2013**, 13, 1743–1750.

(36) Sannomiya, T.; Scholder, O.; Jefimovs, K.; Hafner, C.; Dahlin, A. B. Investigation of Plasmon Resonances in Metal Films with Nanohole Arrays for Biosensing Applications. Small **2011**, 7, 1653–1663.

(37) Alibeigloo, P.; Ghorbanzadeh, M.; Moravvej-Farshi, M. K. Repositioning of Plasmonic Hotspots along the Sidewalls of Conical Nanoholes: A Numerical Investigation. OSA Contin. **2020**, 3, 2817.

(38) Cheng, K.; Wang, S.; Cui, Z.; Li, Q.; Dai, S.; Du, Z. Large-Scale Fabrication of Plasmonic Gold Nanohole Arrays for Refractive Index Sensing at Visible Region. Appl. Phys. Lett. **2012**, 100, 253101.

(39) Wang, J. Q.; Shi, S.; He, R. L.; Yuan, S. F.; Yang, G. Y.; Liang, G. J.; Wang, Q. M. Total Structure Determination of the Largest Alkynyl-Protected fcc Gold Nanocluster $Au_{110}$ and the Study on Its Ultrafast Excited-State Dynamics. J. Am. Chem. Soc. **2020**, 142, 18086–18092.

(40) Han, C.; Li, S. H.; Tang, Z. R.; Xu, Y. J. Tunable Plasmonic Core-Shell Heterostructure Design for Broadband Light Driven Catalysis. Chem. Sci. **2018**, 9, 8914–8922.

(41) Li, W.; Jäckel, F. Size-Controlled Electron Transfer Rates Determine Hydrogen Generation Efficiency in Colloidal Pt-Decorated CdS Quantum Dots. Nanoscale **2018**, 10, 16153–16158.

(42) Li, X.; Bi, W.; Zhang, L.; Tao, S.; Chu, W.; Zhang, Q.; Luo, Y.; Wu, C.; Xie, Y. Single-Atom Pt as Co-Catalyst for Enhanced Photocatalytic $H_2$ Evolution. Adv. Mater. **2016**, 28, 2427–2431.

(43) Ratchford, D. C.; Dunkelberger, A. D.; Vurgaftman, I.; Owrutsky, J. C.; Pehrsson, P. E. Quantification of Efficient Plasmonic Hot-Electron Injection in Gold Nanoparticle-$TiO_2$ Films. Nano Lett. **2017**, 17, 6047–6055.

(44) Hattori, Y.; Meng, J.; Zheng, K.; Meier De Andrade, A.; Kullgren, J.; Broqvist, P.; Nordlander, P.; Sá, J. Phonon-Assisted Hot Carrier Generation in Plasmonic Semiconductor Systems. Nano Lett. **2021**, 21, 1083–1089.

(45) Erwin, W. R.; Zarick, H. F.; Talbert, E. M.; Bardhan, R. Light Trapping in Mesoporous Solar

Cells with Plasmonic Nanostructures. Energy Environ. Sci. **2016**, 9, 1577–1601.

(46) Valenti, M.; Venugopal, A.; Tordera, D.; Jonsson, M. P.; Biskos, G.; Schmidt-Ott, A.; Smith, W. A. Hot Carrier Generation and Extraction of Plasmonic Alloy Nanoparticles. ACS Photonics **2017**, 4, 1146–1152.

(47) Tan, F.; Li, T.; Wang, N.; Lai, S. K.; Tsoi, C. C.; Yu, W.; Zhang, X. Rough Gold Films as Broadband Absorbers for Plasmonic Enhancement of $TiO_2$ Photocurrent over 400-800 Nm. Sci. Rep. **2016**, 6, 1–10.

(48) Tan, F.; Wang, N.; Lei, D. Y.; Yu, W.; Zhang, X. Plasmonic Black Absorbers for Enhanced Photocurrent of Visible-Light Photocatalysis. Adv. Opt. Mater. **2017**, 5, 1600399.

(49) Jia, H.; Wong, Y. L.; Jian, A.; Tsoi, C. C.; Wang, M.; Li, W.; Zhang, W.; Sang, S.; Zhang, X. Microfluidic Reactors for Plasmonic Photocatalysis Using Gold Nanoparticles. Micromachines **2019**, 10, 869.

(50) Zhao, M.; Xu, H.; Ouyang, S.; Tong, H.; Chen, H.; Li, Y.; Song, L.; Ye, J. Fabricating a Au@$TiO_2$ Plasmonic System to Elucidate Alkali-Induced Enhancement of Photocatalytic $H_2$ Evolution: Surface Potential Shift or Methanol Oxidation Acceleration? ACS Catal. **2018**, 8, 4266–4277.

(51) Cesaria, M.; Taurino, A.; Manera, M. G.; Minunni, M.; Scarano, S.; Rella, R. Gold Nanoholes Fabricated by Colloidal Lithography: Novel Insights into Nanofabrication, Short-Range Correlation and Optical Properties. Nanoscale **2019**, 11, 8416–8432.

(52) He, R.; Zhou, X.; Fu, Y.; Zhang, Y. Near-Field Optical Experimental Investigation of Gold Nanohole Array. Plasmonics **2011**, 6, 171–176.

(53) Yue, W.; Wang, Z.; Yang, Y.; Li, J.; Wu, Y.; Chen, L.; Ooi, B.; Wang, X.; Zhang, X. X. Enhanced Extraordinary Optical Transmission (EOT) through Arrays of Bridged Nanohole Pairs and Their Sensing Applications. Nanoscale **2014**, 6, 7917–7923.

(54) Wang, N.; Zhang, X.; Wang, Y.; Yu, W.; Chan, H. L. W. Microfluidic Reactors for

Photocatalytic Water Purification. Lab Chip **2014**, 14, 1074–1082.

(55) Von Rottkay, K.; Rubin, M. Optical Indices of Pyrolytic Tin-Oxide Glass. MRS Proc. **1996**, 426, 449.

(56) Bendavid, A.; Martin, P. J. Review of Thin Film Materials Deposition by the Filtered Cathodic Vacuum Arc Process at CSIRO. J. Aust. Ceram. Soc. **2014**, 50, 86–101.

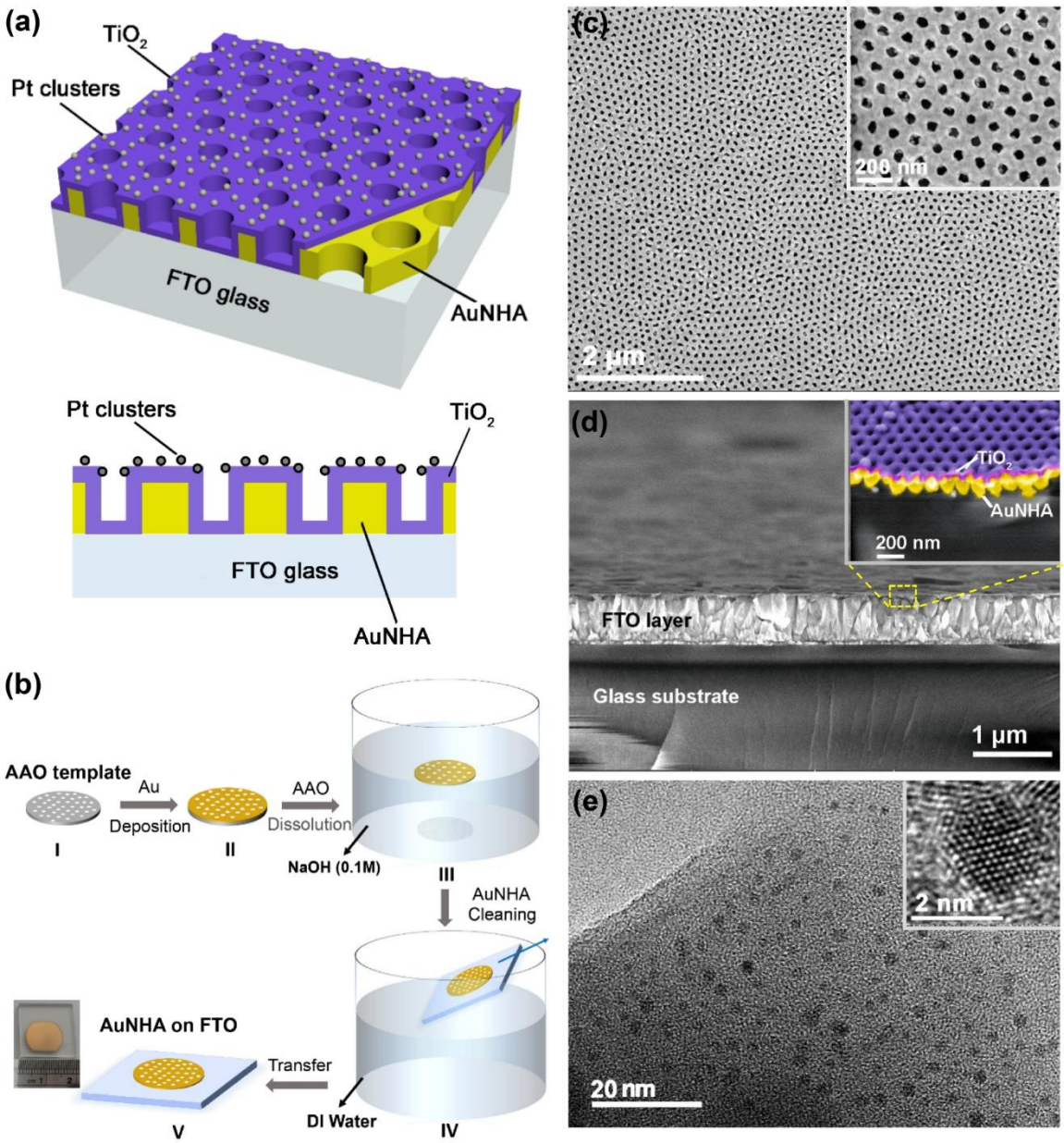


**Figure 1.** (a) The layer structure of Pt/$TiO_2$/AuNHA nanocomposite on the FTO glass. From bottom to top, it has an AuNHA layer (60 nm thick), a $TiO_2$ thin film (15 nm thick) and randomly dispersed Pt nanoparticles. (b) The fabrication procedure of AuNHA on the FTO substrate. (c) The scanning electron microscopic (SEM) images of the AuNHA(D70). The inset presents the close-up SEM image of the AuNHA (D70). (d) The SEM images of the cross-section of the $TiO_2$/AuNHA(D70) bilayer on the FTO substrate. The inset is the close-up of the layer structure, which uses pseudo-colors for easy visualization. (e) The transmission electron microscopic (TEM) image of Pt nanoparticles on the $TiO_2$ layer, the magnified image in the inset shows that the diameter of Pt nanoparticles is about 2 nm.

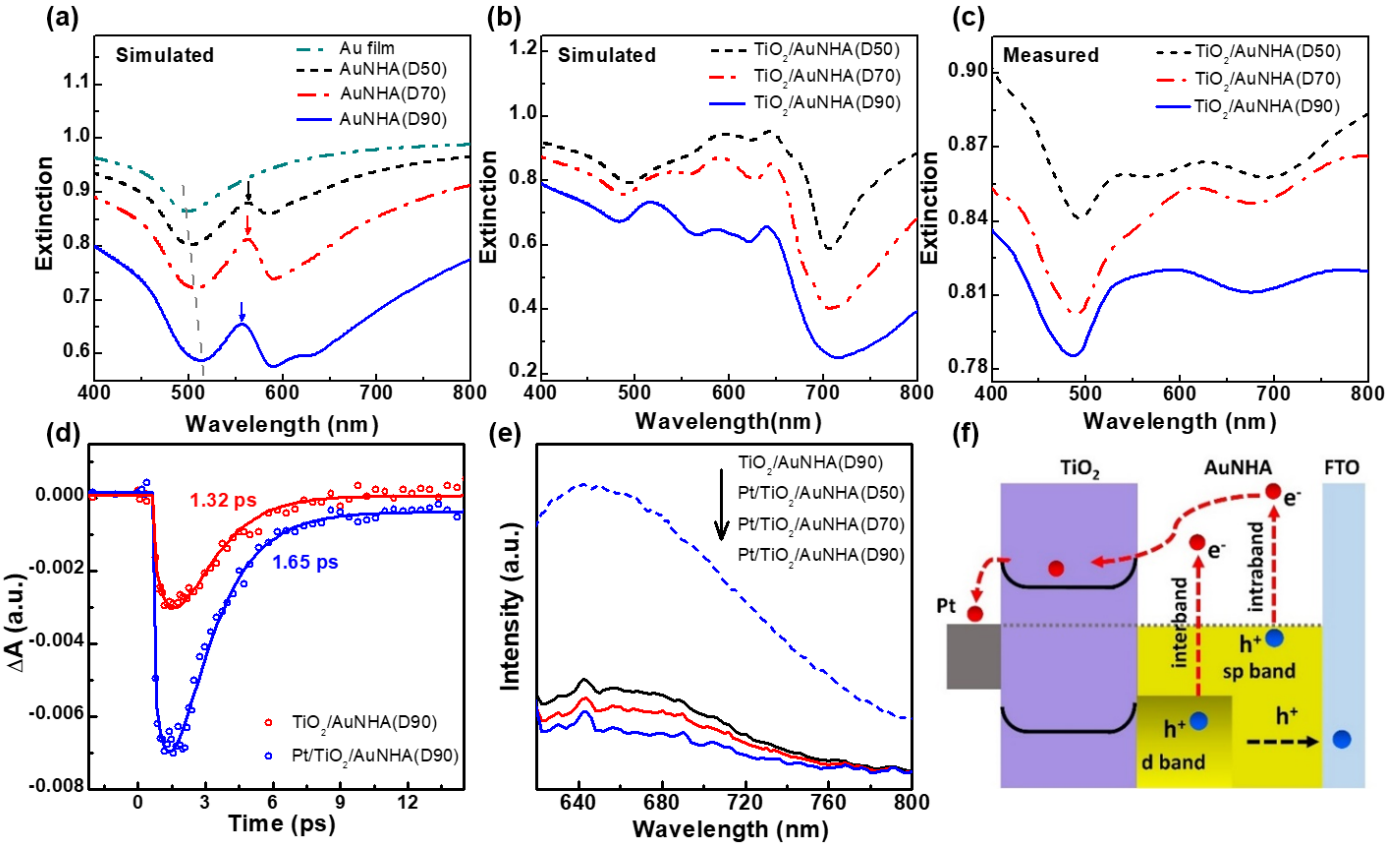


**Figure 2.** (a) The simulated extinction spectra of the Au film and the bare AuNHA (without the $TiO_2$ overlayer) with different hole diameters (50, 70 and 90 nm). (b) Simulated and (c) measured extinction spectra of the $TiO_2$/AuNHA bilayers (without the Pt nanoparticles). Here AuNHA(D50), AuNHA(D70), AuNHA(D90) represent the AuNHA structures with hole diameters of 50, 70, 90 nm, respectively. (d) The bleaching kinetics and the relative fits of $TiO_2$/AuNHA(D90) and Pt/$TiO_2$/AuNHA(D90) at 530 nm obtained from the transient absorption spectra upon the 500-nm excitation. (e) The photoluminescence (PL) spectra of three Pt/$TiO_2$/AuNHA nanocomposites and the $TiO_2$/AuNHA(D90) structure. (f) The energy band diagram of the Pt/$TiO_2$/AuNHA nanocomposite.

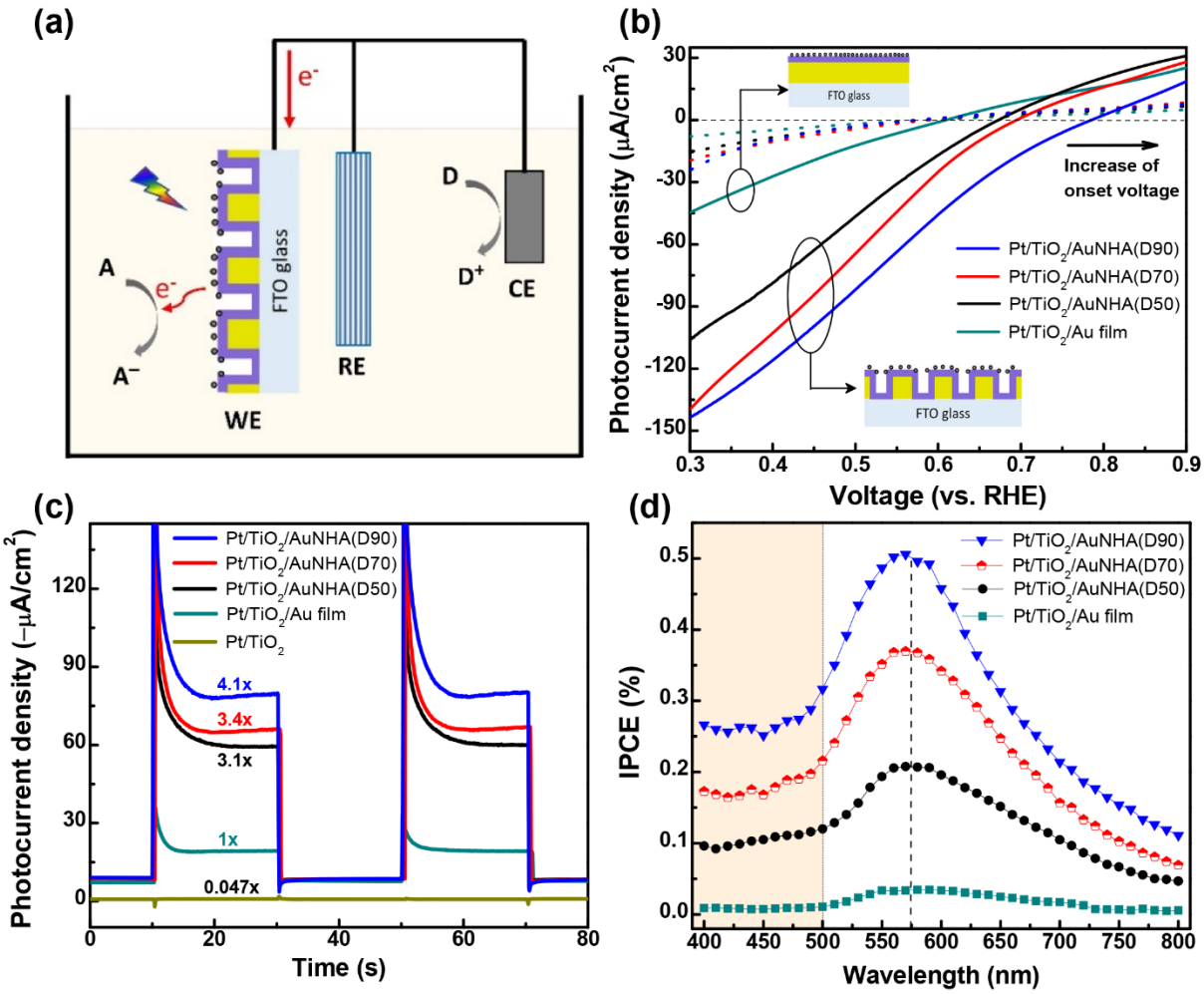


**Figure 3.** (a) The schematic of the photoelectrochemical cell for the experiment. (b–d): Measured results of the linear sweep voltammetry (LSV) curves (b), the transient photocurrent responses (c), and the IPCE (d) as a function of wavelength for the Pt/$TiO_2$/AuNHA nanocomposites and the control samples (i.e., the Pt/$TiO_2$/Au film, the Pt/$TiO_2$ structure). In (a), A and D denote the acceptor and the donor, respectively; and WE, RE and CE represent the working electrode, the reference electrode and the counter electrode, respectively. In (b), the dotted curves represent the measured dark currents, and the cross-points of the LSV curves with the line of $I = 0$ roughly represent the onset voltage, which goes higher with the increase of the nanohole diameter. In (c), the photocurrent density of the bare Pt/$TiO_2$/Au film is used as the reference for easy comparison.

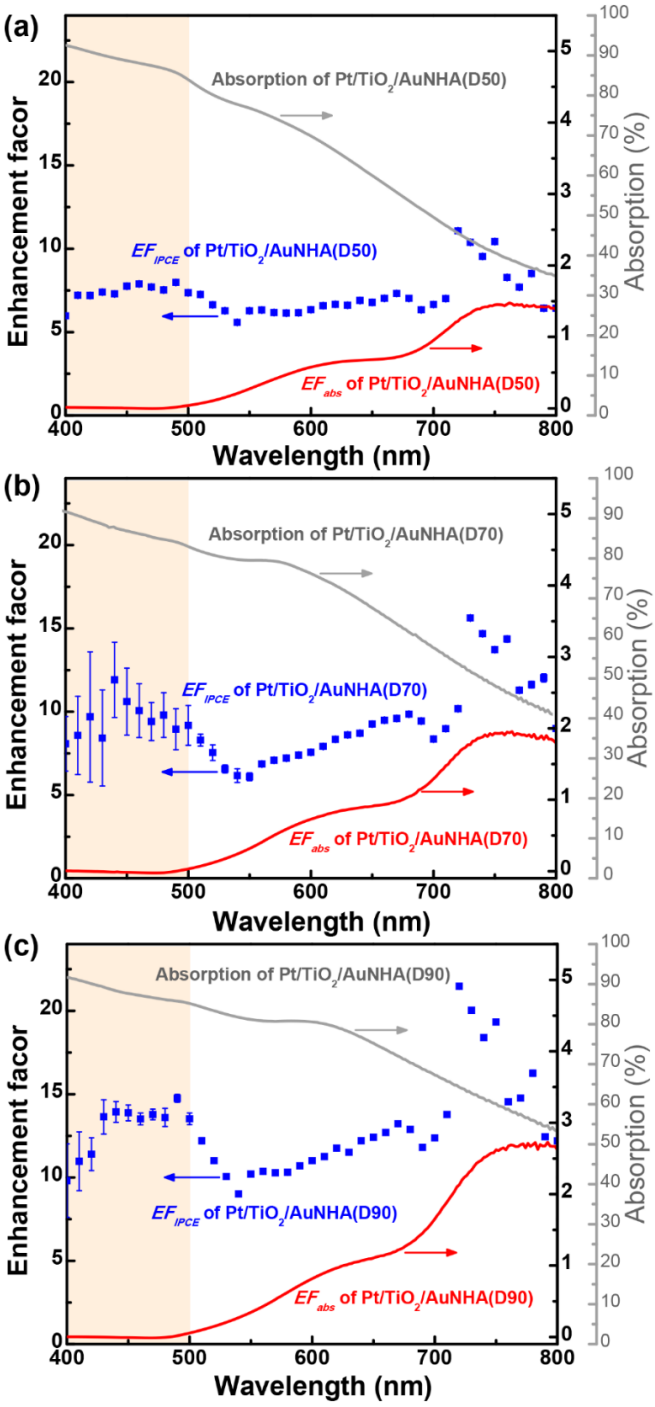


**Figure 4.** The absorption spectra, the enhancement factor of IPCE ($EF_{IPCE}$) and the enhancement factor of absorption ($EF_{abs}$) of the (a) Pt/TiO2/AuNHA(D50), (b) Pt/TiO2/AuNHA(D70), and (c) Pt/TiO2/AuNHA(D90), respectively.

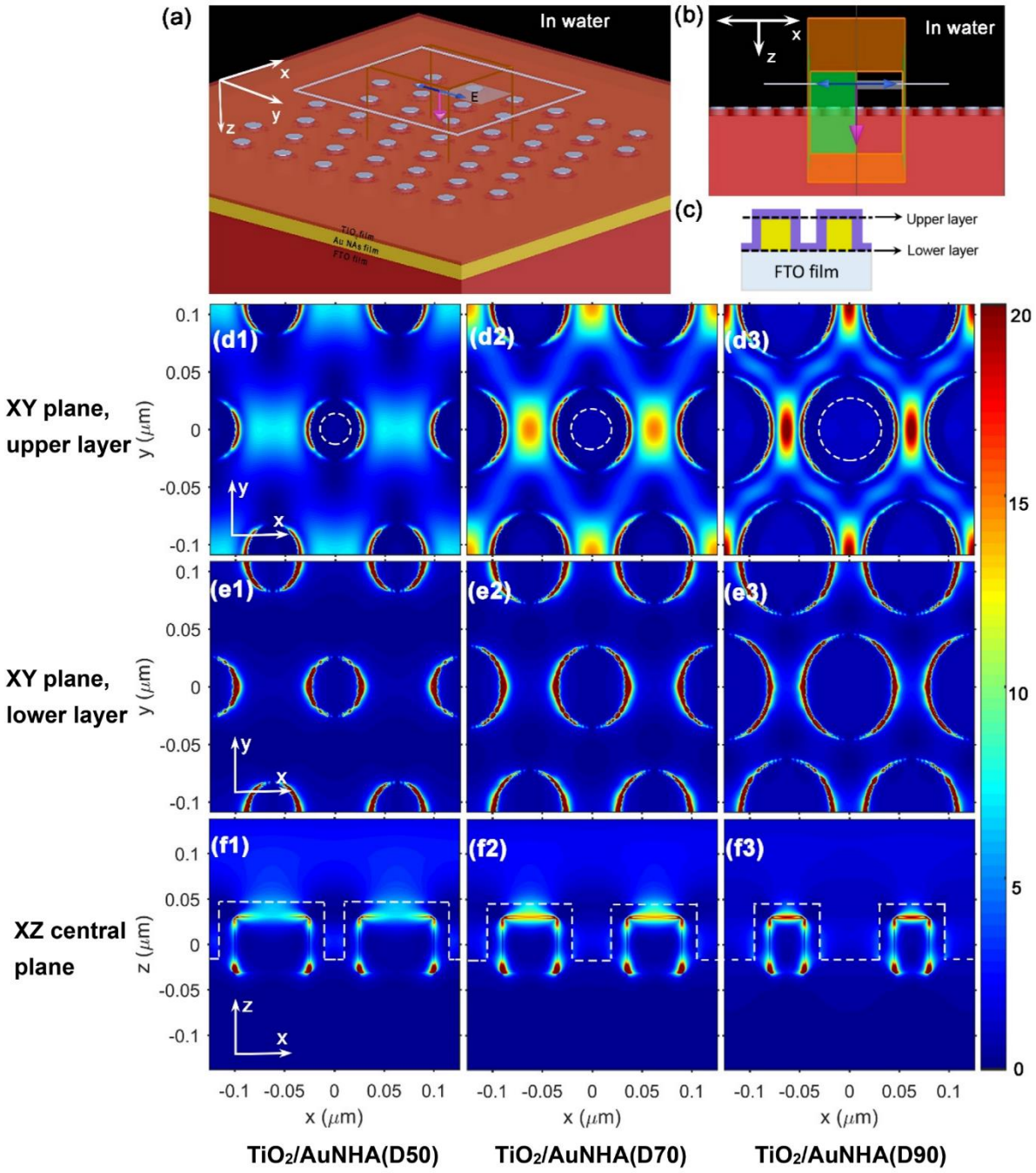


**Figure 5.** (a) Schematic of the $TiO_2$/AuNHA/FTO structure for the FDTD simulation, which consists of an FTO substrate, an AuNHA film in the middle, and a $TiO_2$ overlayer on the top. (b) The XZ view of the unit cell. (c) The XZ view of the hexagonal lattice of the $TiO_2$/AuNHA/FTO structure. The normalized electric field $|E|^2/|E_0|^2$ in the XY plane of the upper layer (d1-d3), the lower layer (e1-e3), and the XZ central plane (f1-f3) for the three $TiO_2$/AuNHA/FTO structures with the hole diameters of 50, 70, 90 nm, respectively. In (d1) – (f3), the surrounding medium is water (not air); and the wavelength is $\lambda$ = 575 nm, which is the position of IPCE peaks of all three samples (see Figure 3d). In (f1) – (f3), the white dotted lines indicate the outer edge of $TiO_2$.

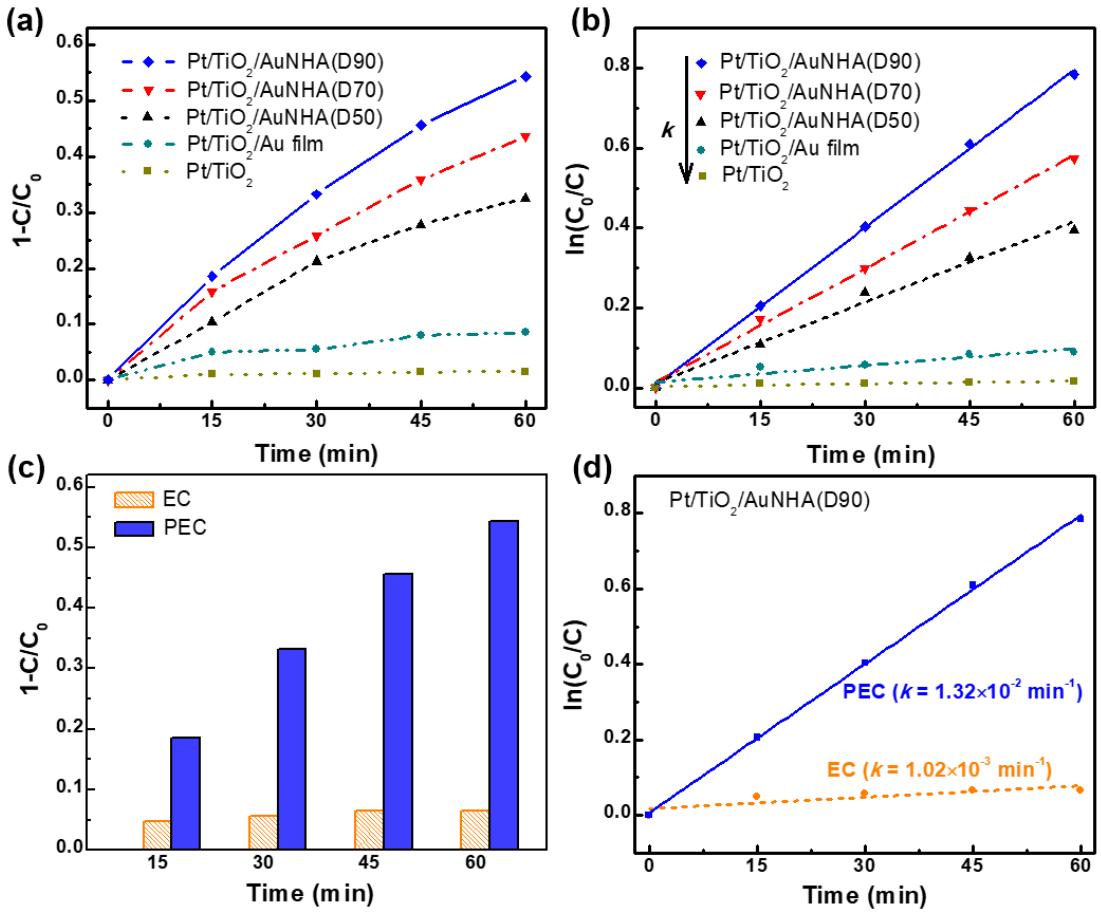


**Figure 6.** (a) The conversion (1–$C/C_0$) and (b) the degradation exponent ln($C_0/C$) as a function of time for the photoelectrocatalytic (PEC) degradation by using the Pt/$TiO_2$ structure, the Pt/$TiO_2$/Au film and the three Pt/$TiO_2$/AuNHA samples. (c) The conversion (1–$C/C_0$) and (d) the degradation exponent ln($C_0/C$) of Pt/$TiO_2$/AuNHA(D90) in the PEC degradation and the electrocatalysis (EC) degradation.

**Table 1.** Comparison of the measured photocatalytic performances of all the prepared samples. The $Pt/TiO_2/Au$ film is used as a reference. The ratios of all the samples are calculated by $S/S_{(Pt/TiO_2/Au\ film)}$. In the measurement, all the applied bias voltage is 0.5 V vs. RHE.

| Sample | Photocurrent density[@] ($\mu A \cdot cm^{-2}$) | Ratio | IPCE[#] | Ratio | Reaction rate constant[&] ($10^{-3}$ $min^{-1}$) | Ratio |
|---|---|---|---|---|---|---|
| **$Pt/TiO_2$/AuNHA(D90)** | **79.4** | **4.1** | **0.50%** | **14.7** | **13.2** | **9.4** |
| $Pt/TiO_2$/AuNHA(D70) | 65.8 | 3.4 | 0.37% | 10.9 | 9.5 | 6.8 |
| $Pt/TiO_2$/AuNHA(D50) | 59.4 | 3.1 | 0.21% | 6.2 | 6.7 | 4.8 |
| $Pt/TiO_2$/Au film | 19.2 | 1.0 | 0.034% | 1.0 | 1.4 | 1.0 |
| $Pt/TiO_2$ | 0.90 | 0.047 | – | – | 0.23 | 0.16 |

[@] Under illumination of visible light ($\lambda$ > 420 nm).
[#] Mean value near the wavelength of 575 nm.
[&] In degrading methyl orange.

**"For Table of Contents Use Only"**

# Plasmonic Nanohole Arrays with Enhanced Visible-light Photoelectrocatalytic Activity

Huaping Jia[1,2,3,4], Zhiyong Li[5], Bingzhe Wang[6], Guichuan Xing[6], Yat Lam Wong[2], Hui Ren[2], Mingjie Li[2], Kwok-Yin Wong[5], Dangyuan Lei[7], Lok-Wing Wong[2], Jiong Zhao[2], Wendong Zhang[1,4], Shengbo Sang[1,4*], Aoqun Jian[1,4*], and Xuming Zhang[2,3*]

[1] Shanxi Key Laboratory of Micro Nano Sensors & Artificial Intelligence Perception, College of Information and Computer, Taiyuan University of Technology, Taiyuan, 030024, China

[2] Department of Applied Physics, The Hong Kong Polytechnic University, Hong Kong, 999077, China

[3] Photonics Research Institute, The Hong Kong Polytechnic University, Hong Kong, 999077, China

[4] Key Lab of Advanced Transducers and Intelligent Control System of the Ministry of Education, Taiyuan University of Technology, Taiyuan, 030024, China

[5] State Key Laboratory of Chemical Biology and Drug Discovery, Department of Applied Biology and Chemical Technology, The Hong Kong Polytechnic University, Hong Kong, 999077, China

[6] Joint Key Laboratory of the Ministry of Education, Institute of Applied Physics and Materials Engineering, University of Macau, Macau, 999078, China

[7] Department of Materials Science and Engineering, City University of Hong Kong, Hong Kong, 999077, China

**TOC Graphics**

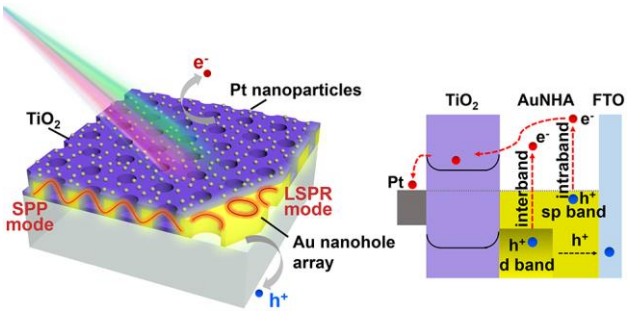


The Pt/$TiO_2$/AuNHA structure as a unique design of photoelectrode exerts both surface plasmon polariton (SPP) and localized surface plasmon resonance (LSPR) simultaneously and exhibits enhanced photoelectrocatalytic performance in visible light.